2nd Advanced Optical Metrology Compendium

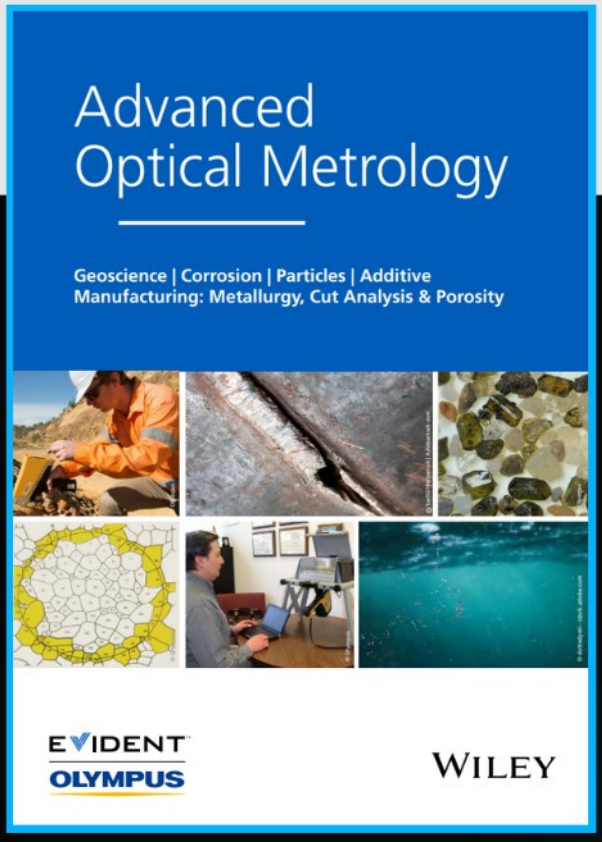

The latest eBook from Advanced Optical Metrology. Download for free.

This compendium includes a collection of optical metrology papers, a repository of teaching materials, and instructions on how to publish scientific achievements.

With the aim of improving communication between fundamental research and industrial applications in the field of optical metrology we have collected and organized existing information and made it more accessible and useful for researchers and practitioners.

EVIDENT
OLYMPUS

WILEY

ADVANCED FUNCTIONAL MATERIALS
www.afm-journal.de

Biotemplating of Metal–Organic Framework Nanocrystals for Applications in Small-Scale Robotics

Anastasia Terzopoulou, Mario Palacios-Corella, Carlos Franco, Semih Sevim, Thomas Dysli, Fajer Mushtaq, María Romero-Angel, Carlos Martí-Gastaldo, De Gong, Jun Cai, Xiang-Zhong Chen, Martin Pumera, Andrew J. deMello, Bradley J. Nelson, Salvador Pané, and Josep Puigmartí-Luis**

Biotemplating is a powerful approach for manufacturing small-scale devices. Here, the assembly of metal–organic framework (MOF) nanocrystals onto biotemplated magnetic helical structures on the cyanobacterium *Spirulina platensis* is reported. It is demonstrated that the authors' approach is universal and can be used to equip biotemplated structures with different functional MOF systems. The successful assembly of MOF nanocrystals on magnetically coated helical biotemplates is achieved by decorating the magnetic surface with gelatin, a naturally occurring macromolecule with synthon moieties that allows anchoring of the MOF nanocrystals via electrostatic interactions. Furthermore, as gelatin is a thermally responsive material, it can serve to free the magnetic biotemplates from the MOF nanocrystal cargoes. As such, the systems can be used as highly integrated magnetically driven microrobots with multiple functionalities. To this end, the potential of these composite helical architectures is demonstrated as MOF-based small-scale robots with applications in biomedicine and environmental remediation.

1. Introduction

The natural world offers a bounty of recurrent architectures at all scales such as spirals, helices, tessellated forms, fractal and dendritic structures, honeycombs, and polyhedral meshes.[1–4] The richness of nature's structures is not a mere result of aesthetics, but of significant functionalities and capabilities. For example, helical structures, which are ubiquitous in nature, can serve various purposes. Usually, a helical arrangement represents a minimum energy configuration that is commonly achieved in dynamic systems via self-assembly of the components forming the helix.[5,6] In certain small organisms, helical appendages can serve as motility components, which allow them to move through fluids in viscous regimes.[7–9]

A. Terzopoulou, C. Franco, S. Sevim, T. Dysli, F. Mushtaq, X.-Z. Chen, B. J. Nelson, S. Pané
Institute of Robotics and Intelligent Systems
ETH Zurich
Tannenstrasse 3, Zurich CH-8092, Switzerland
E-mail: vidalp@ethz.ch

M. Palacios-Corella, M. Romero-Angel, C. Martí-Gastaldo
Instituto de Ciencia Molecular
Universidad de Valencia
Catedratico Jose Beltran 2, Paterna 46980, Spain

M. Palacios-Corella, M. Pumera
Future Energy and Innovation Laboratory
Central European Institute of Technology
Brno University of Technology
Brno 61200, Czech Republic

The ORCID identification number(s) for the author(s) of this article can be found under https://doi.org/10.1002/adfm.202107421.

DOI: 10.1002/adfm.202107421

D. Gong, J. Cai
School of Mechanical Engineering and Automation
Beihang University
No. 37 Xueyuan Road, Haidian District, Beijing 100191, China

M. Pumera
3D Printing & Innovation Hub
Department of Food Technology
Mendel University in Brno
Brno 61300, Czech Republic

M. Pumera
Department of Medical Research
China Medical University Hospital
China Medical University
Taichung 40402, Taiwan

A. J. deMello
Institute for Chemical and Bioengineering
ETH Zurich
Tannenstrasse 3, Zurich CH-8092, Switzerland

J. Puigmartí-Luis
Departament de Ciència dels Materials i Química Física
Institut de Química Teòrica i Computacional
Barcelona 08028, Spain
E-mail: josep.puigmarti@ub.edu

J. Puigmartí-Luis
ICREA
Institució Catalana de Reserca i Estudis Avançats
Pg. Lluís Companys 23, Barcelona 08010, Spain

Several fields of research and engineering use nature as a source of inspiration to create and develop artificial systems with bespoke shape and performance.[10–13] For example, the field of small-scale robotics has unquestionably been inspired from the shape of motile organs of microorganisms and cells.[14–16] In his famous lecture "Life at low Reynolds number",[17] Purcell identified the main mechanisms that small living entities use to swim through fluids, and concluded that, in order to propel, these organisms realize non-reciprocal motions, such as beating a flexible oar or rotating a chiral appendage. Several organisms have exploited helical shapes to swim through fluids. Such organisms display either helical flagella,[18,19] or an entire helical body,[20] which they rotate to generate a translational corkscrewing propulsion mechanism.[8] Inspired by such a strategy, small-scale roboticists have developed processes to manufacture micro- and nano-helices[21–23] for applications in biomedicine[24–26] and environmental remediation.[27–30] While a great body of small-scale robotics research has been dedicated to building artificial versions of nature, other investigations have exploited biological structures as templates or scaffolds to engineer robotic devices or machinery.[31–34] In this approach, known as biotemplating, the synthesis of a morphologically controlled material is directed by the underlying biological architecture. Owing to its high versatility, biotemplating offers an interesting alternative to top-down micro- and nanofabrication techniques (e.g., laser writing,[35,36] glancing angle deposition,[37] or advanced photolithography[38]). The use of natural constructs not only enables more sustainable solutions for large-scale fabrication of systems,[39] but also benefits from optimized shapes and materials with the level of sophistication required for the realization of small-scale devices.[40]

Herein, we present a universal biotemplating approach that uses naturally occurring helical architectures to obtain controlled 3D assemblies of nanocrystalline metal–organic frameworks (MOFs). Our process exploits *Spirulina platensis*,[41] a filamentous cyanobacteria with a helical body, which provides the shape of the final composite microstructure. Next, we create a magnetic helical chassis on top of the *S. platensis*,[42] which is subsequently coated with various MOF nanocrystals. The resulting composite helical structure is a highly integrated, magnetically driven MOF-based microrobot (MOFBOT).[43,44] Our approach is successfully demonstrated with the following MOF nanocrystals (Figure S1, Supporting Information): Matériaux de l'Institut Lavoisier (MIL)-100(Fe) (17 ± 2 nm),[45] MIL-125NH_2 (93 ± 34 nm),[46] Universitetet I Oslo (UiO)-66 (73 ± 12 nm),[47] and zeolitic imidazolate framework (ZIF)-8 (755 ± 52 nm),[48a] hereafter called MIL-100(Fe)@MOFBOTs, MIL-125NH_2@MOFBOTs, UiO-66@MOFBOTs, and ZIF-8@MOFBOTs, respectively. To ensure a homogenous coverage of the bio-templated magnetic chassis by MOF nanocrystals, the magnetic surface is functionalized with a thin layer of glycerol-plasticized gelatin. This organic layer additionally serves as a thermally-responsive component, which allows the controlled release of the assembled MOF nanocrystals (**Figure 1**a). Our approach allows the production of MOFBOTs via simple fabrication steps, combining bio-templating and self-assembly processes. The resulting microrobots integrate magnetic locomotion capabilities with the specific chemistry associated to each MOF system. Finally, as a proof-of-concept, we utilize our MIL-100(Fe)@MOFBOTs to achieve targeted drug delivery in cancerous cells (Figure 1b), and MIL-125NH_2@MOFBOTs to perform photocatalytic degradation of an organic pollutant in water (Figure 1c). More generally, we show that our scalable bio-templated approach can serve as a powerful tool to design MOFBOTs for various applications in fields ranging from biomedicine to environmental remediation.

2. Results and Discussion

The fabrication protocol used for the production of our biotemplated MOFBOTs is illustrated in **Figure 2**a. We selected *S. platensis*, a filamentous cyanobacterium with helical shape, to serve as the biotemplate for the synthesis of the MOFBOTs. First, we coated the *S. platensis* with pre-synthesized magnetic iron oxide nanoparticles by simply immersing the helical biotemplates in a solution of iron oxide nanoparticles. The assembly was then annealed to eliminate the organic biotemplate, resulting in pure magnetic helical microstructures. Next, we decorated the surface of the magnetic helical microstructures with a responsive glycerol-plasticized gelatin coating. Carboxylic and amine groups in gelatin act as a supramolecular synthon allowing the coordination of metal ions. Hence, in the last step, the MOF nanocrystals were anchored to the magnetic templates via their supramolecular interaction with the gelatin layer. The evolution of the surface morphology of the biotemplate over the various fabrication steps is depicted in the scanning electron microscopy (SEM) images presented in Figure 2b–e. After coating the surface of the *S. platensis* with magnetic iron oxide nanoparticles, it is possible to observe the nanoparticulate texture of the magnetic coating (Figure 2c). Remarkably, the helical shape of the homogeneously covered biotemplates was preserved during the annealing process, resulting in magnetic helical microstructures with a hollow core (see Figure 2d; Figure S2, Supporting Information, respectively). Interestingly, while the roughness of the magnetic helical templates preserves the original texture of the *S. platensis*, the coating with the MOF nanocrystals completely changes their surface morphology, increasing not only their roughness but also their overall thickness (Figure 2e; Figure S3, Supporting Information). These results clearly confirm the efficiency of the glycerol-plasticized gelatin approach for bonding MOF nanocrystals to the magnetic helical microstructures. It should be noted, that the magnetic helical templates are completely covered with the MOF nanocrystals as shown in the SEM images presented in Figure 2e. While other groups have demonstrated the coating of living organisms with MOF crystals,[48b,c] the resulting structures do not show controlled locomotion capabilities.

To demonstrate that our biotemplated approach is broadly applicable to a range of MOFs, with different chemical compositions and crystal structures, we prepared biotemplated MOFBOTs such as MIL-100(Fe)@MOFBOTs, MIL-125NH_2@MOFBOTs, UiO-66@MOFBOTs, and ZIF-8@MOFBOTs. **Figure 3**a–d shows SEM images of the biotemplated MOFBOTs, alongside energy-dispersive X-ray spectroscopy (EDX) maps. Using the EDX maps, we verified the presence of the metal ions characteristic for each MOF system, namely Fe for MIL-100(Fe), Ti for MIL-125NH_2, Zr for UiO-66, and Zn for ZIF-8. Additionally, Fourier-transform infrared spectroscopy (FTIR) was used to characterize the biotemplated MOFBOTs. It can be

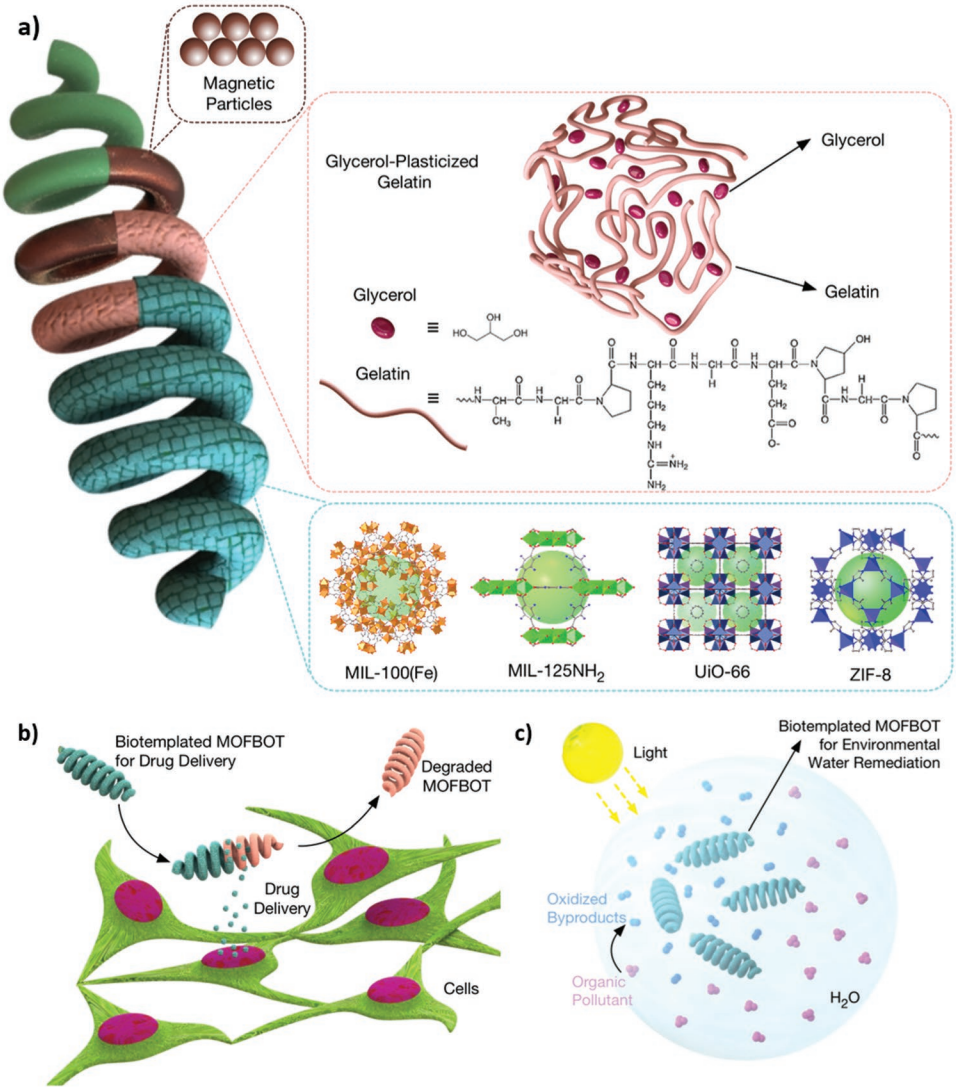

Figure 1. a) Illustration of a biotemplated MOFBOT including all its components. Schematic drawings of: b) drug delivery with MIL-100(Fe)@MOFBOTs and c) water remediation with MIL-125NH_2@MOFBOT.

seen that the FTIR spectra acquired from each MOFBOT shows the characteristic peaks of iron oxide, and Fe—O stretching band at ≈580 cm^{-1},[49] as well as of the respective MOF system (Figure S4, Supporting Information). While MIL-100(Fe)@MOFBOTs, MIL-125NH_2@MOFBOTs, and UiO-66@MOFBOTs show intense bands around 1600–1500 cm^{-1} and 1450–1370 cm^{-1}, assigned to asymmetric and symmetric vibrations of the carboxylic groups, respectively, the small band at 800 cm^{-1} in MIL-125NH_2@MOFBOTs was undoubtedly assigned to the Ti—O—Ti—O vibration mode of the MIL-125NH_2 nanoscrystals,[50] and the sharp band at 550 cm^{-1} in UiO-66@MOFBOTs was ascribed to the Zr—(OC) asymmetric stretching vibration of the UiO-66 nanoscrstals.[51] In ZIF-8@MOFBOTs, the bands located at 1420,1140, and 1000 cm^{-1} were assigned to the C—N stretching vibration and the bands around 1500 and 1250 cm^{-1} were attributed to the stretching of the imidazole ring.[52] These data further confirm the integration of the MOF nanocrystals with the magnetic helical microstructures. To demonstrate the preservation of the crystalline structure of the MOF nanocrystals and of the magnetic template during the fabrication process, we performed X-ray diffraction (XRD) analysis. As shown in Figure 3e–h, we compared the XRD patterns of the bare MOF nanocrystals with the biotemplated MOFBOTs and the magnetic helical structures. Significantly, the XRD patterns for each biotemplated MOFBOT system exhibit characteristic peaks of the respective MOF (at angles $2\theta < 25°$) as well as of the iron oxide present in the magnetic helical structure (at angles 2θ equal to 24°, 30°, 33°, and 35.5°).

Owing to their magnetic properties and helical shape, the synthesized biotemplated MOFBOTs are equipped with magnetic locomotion capabilities. Under the application of external magnetic fields, the MOFBOTs can be remotely navigated along a controlled trajectory and swim to a region of interest. A time lapse overlay image of a biotemplated MOFBOT guided on a M-shaped trajectory is shown in Figure S5a, Supporting Information. The velocity of the MOFBOT is strongly dependent on the rotational frequency of the field. At low frequencies (i.e., between 1 and 5 Hz), a wobbling locomotion scheme

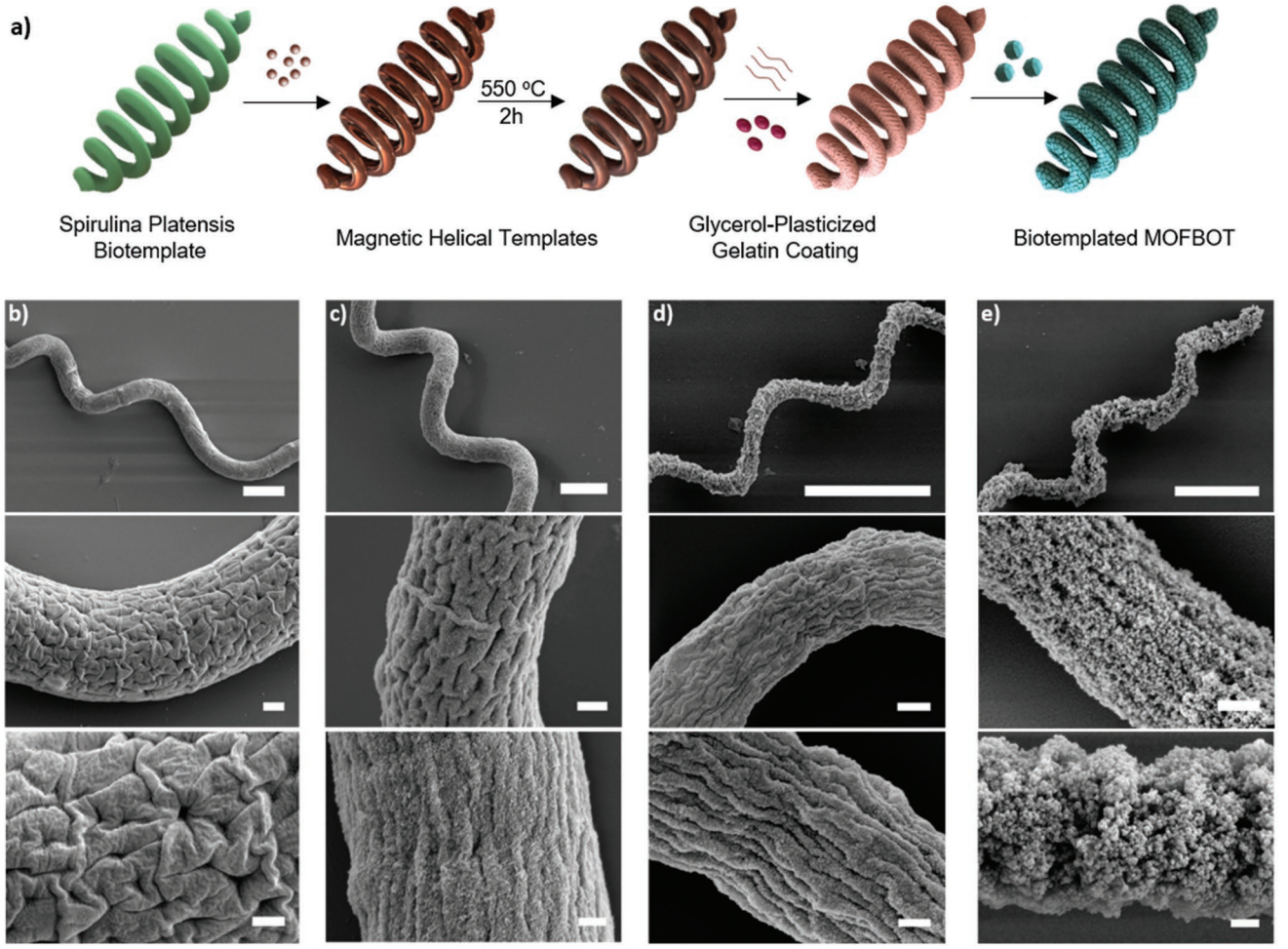

Figure 2. a) Fabrication steps followed to achieve biotemplated MOFBOTs and the corresponding SEM images of: b) biotemplates, c) coated biotemplates, d) magnetic helical templates after annealing, and e) biotemplated MOFBOTs, here MIL-125NH_2@MOFBOTs. Scale bars; top row 10 µm, middle row 1 µm, and bottom row 500 nm.

was observed, whilst at higher frequencies (i.e., between 6 and 16 Hz), corkscrew forward locomotion was the dominant propulsion mechanism (Video S1, Supporting Information). The maximum velocity of the MOFBOT was achieved using a frequency of 17 Hz, which was identified as the step-out frequency beyond which the magnetic locomotion rapidly decreases (Figure S5b, Supporting Information).

Once we demonstrated the capacity of the described biotemplated approach for the efficient integration of MOF nanocrystals onto magnetically-guided helical structures, we investigated the utility of the resulting structures (i.e., the biotemplated MOFBOTs) in the context of two highly relevant edge applications, namely biomedicine and water remediation. Specifically, MIL-100(Fe)@MOFBOTs were investigated as a promising drug delivery system (Figure 1b), while MIL-125NH_2@MOFBOTs were studied as potential agents for the removal of organic pollutants from water (Figure 1c).

Remote navigation of magnetic microrobots is considered to be one of the least invasive and most promising techniques for targeted drug delivery tasks.[53] Magnetic MOFBOTs hold great promise in this field, due to the large drug encapsulation efficiencies of MOF crystals.[54,55] Specifically, MIL-100(Fe) has been already reported as a good carrier of therapeutic molecules due to its high drug loading capacity and excellent biocompatibility properties.[56,57] We chose the cancer therapeutic drug doxorubicin (DOX) to test the efficacy of MIL-100(Fe)@MOFBOTs as a drug delivery carrier. We first investigated the drug loading capacity of the MIL-100(Fe) nanocrystals. The MIL-100(Fe) nanocrystals were synthetized following a recently described methodology.[45] DOX was loaded to the MIL-100(Fe) nanocrystals by a simple incubation of the as-synthesized nanoscale crystals in a DOX solution in water (see the Supporting Information for further details). The drug loading capacity of the system was estimated at 100 µg of DOX per mg of MOF nanocrystals. The XRD patterns of the MIL-100(Fe) nanocrystals before and after DOX loading are shown in **Figure 4**a, where no significant differences are apparent. Next, we investigated the effectiveness of the DOX@MIL-100(Fe) nanocrystals as drug delivery agents in vitro. The results of cell viability after a 24-h incubation with MDA-MB-231 cancer cells, are shown in Figure S6a, Supporting Information. We observed that DOX@MIL-100(Fe) nanocrystals could act as effective drug carriers even at concentrations as low as 20 µg mL^{-1}, killing ≈90% of the cell culture. In sharp contrast, cell cultures treated with pristine MIL-100(Fe)

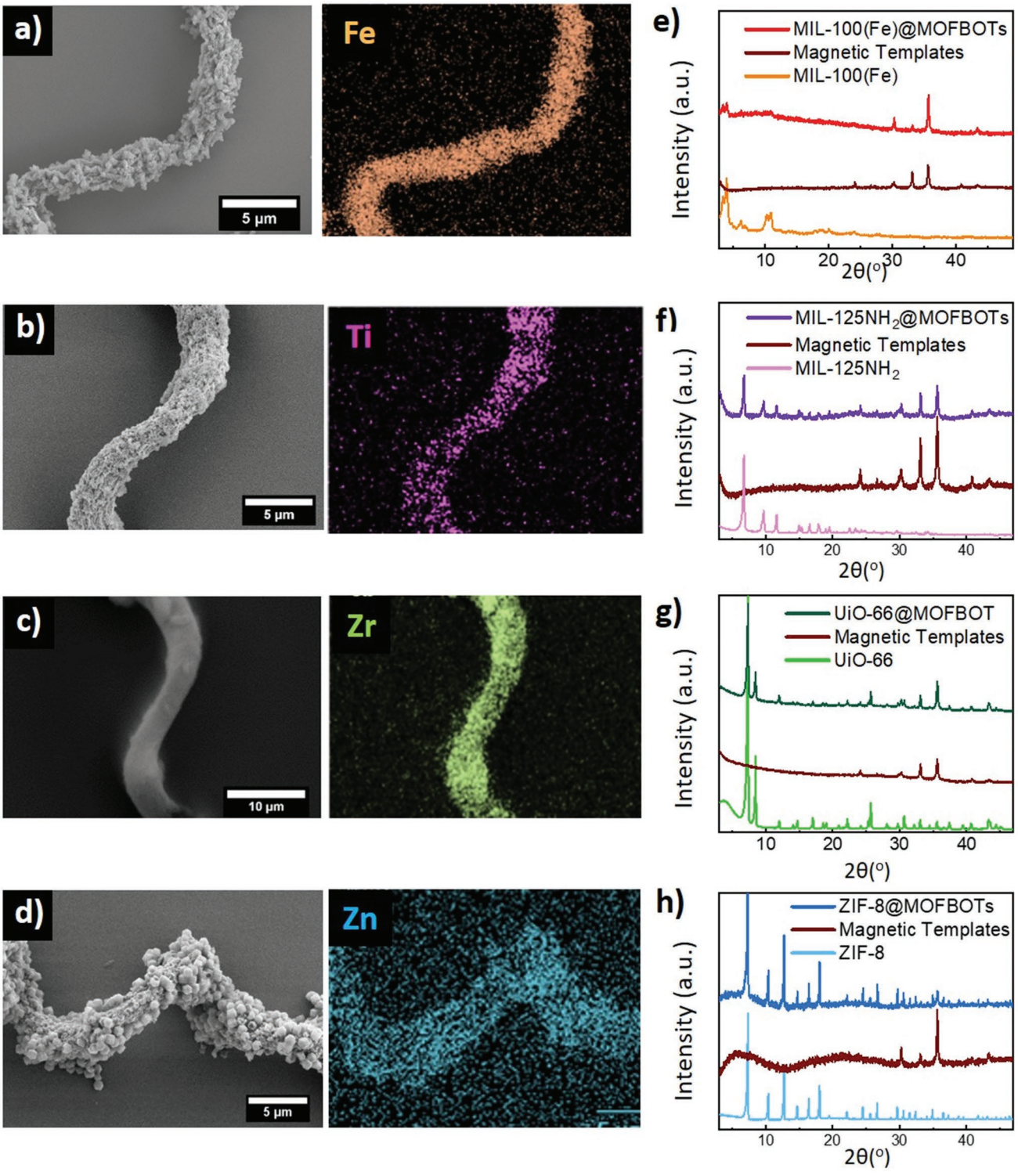

Figure 3. SEM images and EDX maps of the biotemplated MOFBOTs and their characteristic metals: a) Fe for MIL-100(Fe)@MOFBOTs, b) Ti for MIL-125NH_2@MOFBOTs, c) Zr for UiO-66@MOFBOTs, and d) Zn for ZIF-8@MOFBOTs. e–h) Comparative XRD patterns of the respective MOF nanocrystals, magnetic templates, and biotemplated MOFBOTs.

nanocrystals at the same concentration showed up to 90% cell viability. The optical and fluorescence microscopy images, with a LIVE/DEAD stain, clearly show this effect, with a large population of dead cells (cells stained in red) at the cell culture incubated with DOX@MIL-100(Fe) nanocrystals (Figure S6b,c, Supporting Information). Based on these results, we prepared

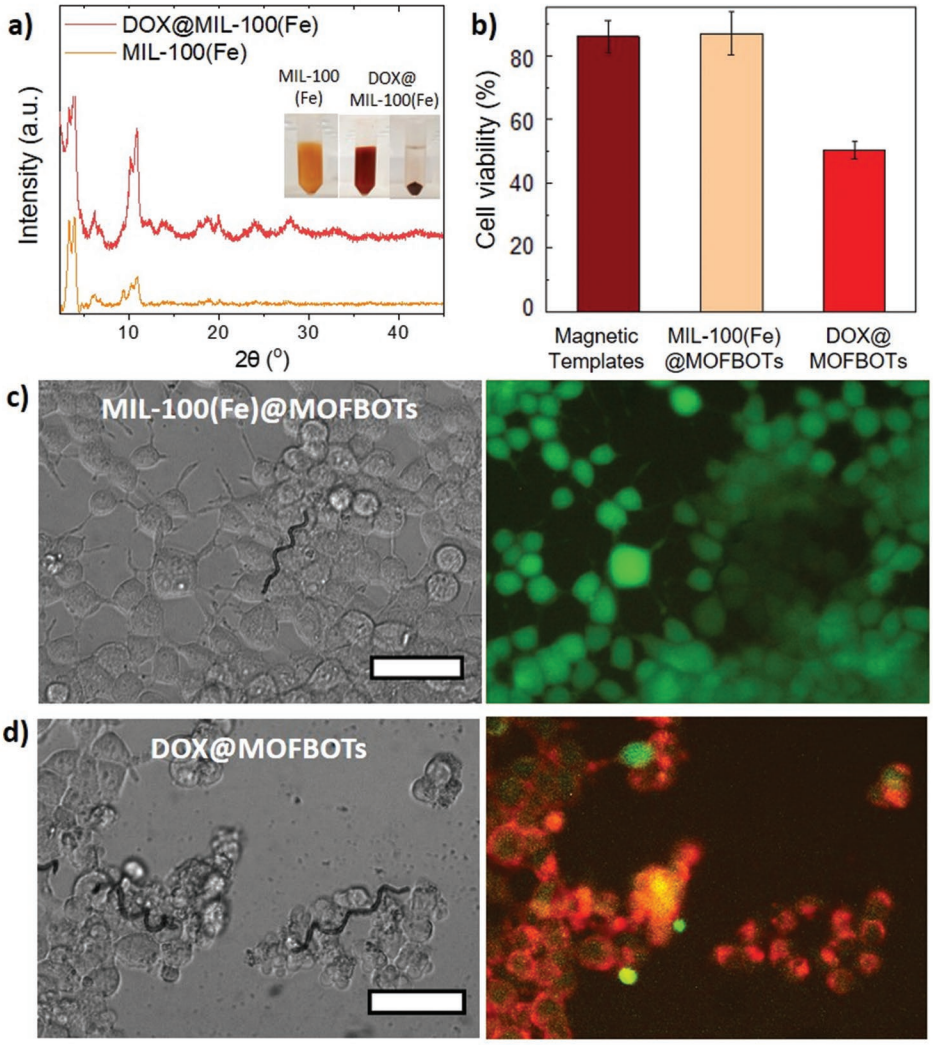

Figure 4. a) XRD patterns of MIL-100(Fe) and DOX loaded MIL-100(Fe) nanocrystals; inset shows dispersions of MIL-100(Fe) nanocrystals before and after DOX loading. b) Cell viability (%) in MDA-MB-231 cell cultures treated with magnetic templates, MIL-100(Fe)@MOFBOTs, and DOX@MOFBOTs. Optical and fluorescence (LIVE/DEAD stain) microscopy images of cells treated with c) MIL-100(Fe)@MOFBOTs and d) DOX@MOFBOTs. Scale bars in the optical microscopy images, 50 µm.

the biotemplated MOFBOTs equipped with DOX@MIL-100(Fe) nanocrystals (hereafter DOX@MOFBOTs) and used them as targeting drug delivery agents.

The efficacy of DOX@MOFBOTs as targeting drug delivery agents was investigated in a cell culture of MDA-MB-231 cells. We observed that cell viability remained above 80% when the cells were treated with the magnetic helical templates or MIL-100(Fe)@MOFBOTs, while, it dropped below 50% in the presence of DOX@MOFBOTs, Figure 4b. The optical and fluorescence microscopy images, with LIVE/DEAD stain, clearly show this effect, with dead cells (cells stained in red) surrounding DOX@MOFBOTs, Figure 4c,d.

The proposed mechanism of action for local drug delivery with DOX@MOFBOTs involves the dissolution of the gelatin layer when the MOFBOTs are incubated with the cells at 37 °C. This effect is clearly visible when imaging the surface of MIL-100(Fe)@MOFBOTs before and after incubation with cells (Figure S7, Supporting Information). Indeed, after 24 h of incubation in a cell culture, the MOF nanocrystals disappear. The dissolution of the glycerol-plasticized gelatin coating results in a stimuli responsive release of MIL-100(Fe) nanocrystals from the magnetic helical template, allowing them to further interact with the surrounding cells. This mechanism of action highlights the importance of the gelatin layer as a responsive element triggering the release of MOF nanocrystals. In this regard, it should be noted that this biotemplating approach clearly leads to the manufacturing of a highly integrated microrobotic system for controlled drug delivery applications.

To highlight potential applications of biotemplated MOFBOTs beyond the field of biomedicine, we explored the feasibility of using biotemplated MOFBOTs in water remediation. In this context, we chose MIL-125NH_2@MOFBOTs. MIL-125NH_2 is known for its photocatalytic activity.[58] MIL-125NH_2 can absorb visible light (550 nm), as its bandgap is ≈2.6 eV,[59] and accordingly, under UV–vis irradiation, electron–hole pairs can be generated, which react with water molecules, or hydroxide

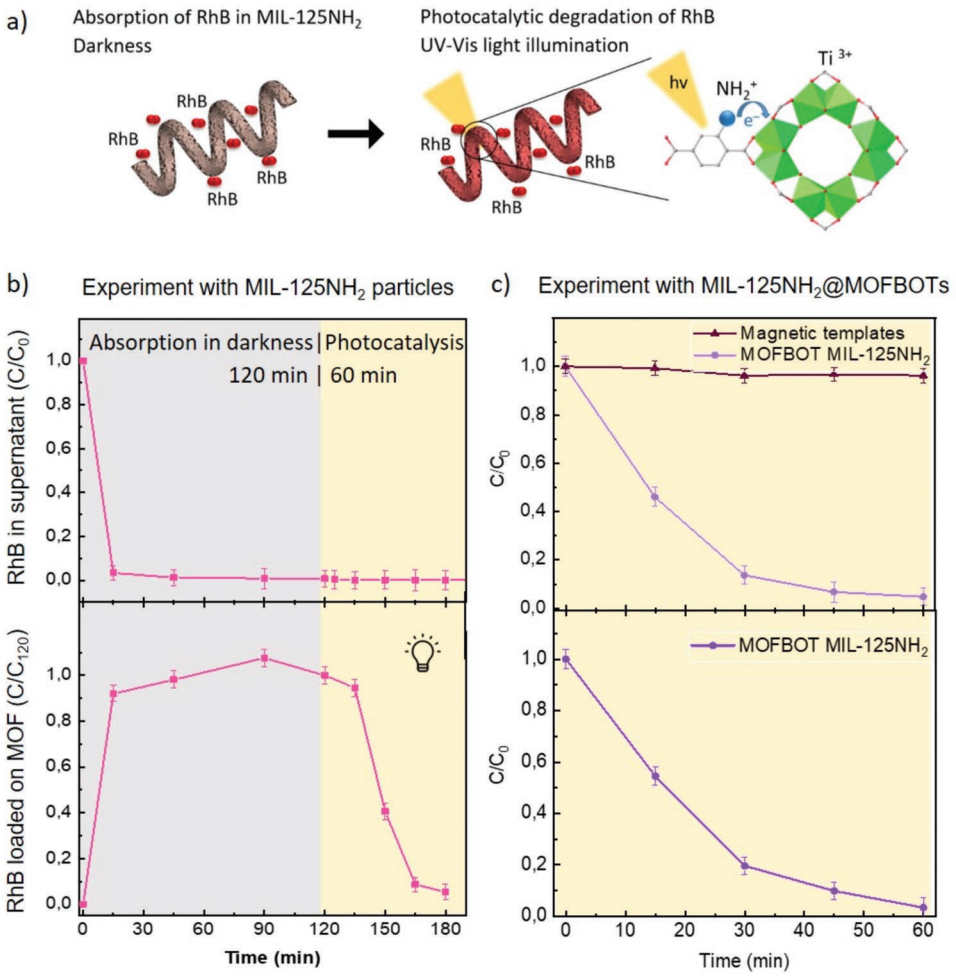

Figure 5. a) Schematic illustration of the photocatalytic degradation experimental procedure, showing the two processes, absorption (in darkness) and photocatalysis (under UV–vis illumination). b) Normalized RhB concentration in the supernatant solution during absorption and phototcatalysis experiment with MIL-125NH_2 nanocrystals and normalized RhB concentration absorbed in the MIL-125NH_2 nanocrystals during absorption and phototcatalysis experiment. c) Normalized RhB concentration in the supernatant solution during phototcatalysis experiment with MIL-125NH_2@MOFBOTs and normalized RhB concentration absorbed in the MIL-125NH_2@MOFBOTs during the phototcatalysis experiment.

ions, to produce hydroxyl (•OH) radicals. The formation of active •OH radicals is required as the first step in the degradation of organic pollutants via consecutive redox reactions.[60]

As a proof-of-concept, we employed our MIL-125NH_2@MOFBOTs for the removal of organic pollutants from water. We chose Rhodamine B (RhB) as a model organic pollutant of water. It is important to note that when introducing a porous material in a solution of RhB, the dye can also be absorbed in the pores. This process played a significant role in our investigations, as large amounts of RhB were absorbed in the pores of the nanoscale MIL-125NH_2 crystals. To discriminate the two processes, that is, absorption and photocatalysis, we performed all experiments in two steps; first, the incubation of the nanoscale MIL-125NH_2 crystals in a RhB solution (15 mg L^{-1}) over 120 min in darkness, and second, photocatalysis under UV–vis light illumination for 60 min (**Figure 5**a). Initial experiments used MIL-125NH_2 nanocrystals. At each time point, we measured the RhB concentration in the supernatant solution and the amount of RhB absorbed in the MIL-125NH_2 nanocrystals (see the Experimental Section). As illustrated in Figure 5b (top), the concentration of RhB in the supernatant solution drops dramatically due to simple absorption of the dye (in darkness) into the pores of the MIL-125NH_2 nanocrystals. This observation is verified as the amount of RhB encapsulated in the MOF crystals increases over time (Figure 5b (bottom)). After 120 min of incubation in darkness, we irradiated the sample with UV–vis light. The results show that after 60 min of photocatalysis, more than 90% of the RhB degraded, including the proportion encapsulated in the MOF nanocrystals.

Once the capacity of the MIL-125NH_2 nanocrystals to degrade RhB was demonstrated, we further investigated the photocatalytic activity of MIL-125NH_2@MOFBOTs. Following the protocol previously established, we incubated MIL-125NH_2@MOFBOTs in a RhB solution (10 mg L^{-1}) in darkness before illumination. Figure 5c (top) illustrates the RhB concentrations in the supernatant solution over the time of the photocatalysis experiment. We clearly observed the degradation of RhB in the presence of MIL-125NH_2@MOFBOTs (purple line), while the concentration of RhB remained stable in control experiments, that is, when exposed to pristine magnetic helical templates (brown

line). Figure 5c (bottom) shows the amount of RhB absorbed in the MIL-125NH_2@MOFBOTs during the photocatalysis experiment. Accordingly, it can be concluded that both RhB in the surrounding solution as well as RhB absorbed in MIL-125NH_2 nanocrystals are degraded during the photocatalysis experiment. Remarkably, the MIL-125NH_2@MOFBOTs remained intact during the photocatalysis experiments as demonstrated by the SEM images in Figure S8, Supporting Information. With these results, we confirm that MIL-125NH_2@MOFBOTs are excellent candidates for photocatalytic degradation of organic pollutants, such as RhB, present in water.

3. Conclusion

Herein, we have presented a universal biotemplating-based methodology to fabricate 3D helical assemblies of MOF nanocrystals. Specifically, *S. platensis* is used as a biotemplate on which multiple components comprising a magnetic chassis, a gelatin binder film, and a MOF nanocrystal coating are assembled. The key to our approach is the integration of a film containing a macromolecular binder with synthon moieties (in this case, gelatin) that allows for the controllable organization via electrostatic interactions of MOF nanocrystals around the 3D helical biotemplated structure. The binder enables the incorporation of virtually any MOF nanosystem (in this contribution, MIL-100(Fe), MIL-125NH_2, UiO-66, and ZIF-8). To highlight the potential of these composite 3D architectures, we demonstrate their use as magnetically driven MOF-based robots (MOFBOTs). Taking advantage of the specific chemistry associated with each MOF system, we are able to tune the MOFBOTs to the application of interest. MIL-100(Fe)@MOFBOT is used to perform microrobotic targeted drug delivery in cancer cells, and MIL-125NH_2@MOFBOT, to perform photocatalytic degradation of an organic pollutant in water. The countless possibilities of our newly introduced biotemplated MOFBOTs fabrication method are only matched by the amount of different MOF systems and their specific properties. This conceptual approach of designing of MOF systems via biotemplating shall find a broad scope of applications in microrobotics systems and beyond.

4. Experimental Section

Synthesis of Biotemplated MOFBOTs: All chemicals were purchased from Sigma–Aldrich, unless indicated otherwise. Below, we describe the fabrication protocols for the various MOF particles as well as the corresponding biotemplated MOFBOTs.

MIL-100(Fe) particles were prepared following the synthesis reported by Franco et al.[45] Briefly, in 61 mL of SDS solution (0.1 M), 40.2 mg NaOH and 70.4 mg trimesic acid, along with 2 mL of cetyltrimethylammonium bromide (CTAB) solution (0.1 M) were added under stirring. This mixture was combined with a second solution of 42 mL of sodium dodecylsulfate (SDS) (0.1 M), 100 mg $FeCl_2$, and 1 mL CTAB (0.1 M). The reaction occured at room temperature and overnight, with the final product being precipitated the day after by addition of 100% of ethanol. The final product was collected after several wash steps with ethanol.

MIL-125NH_2 nanoparticles were prepared following a recently reported procedure.[46] 2-aminoterephtalic acid (274.5 mg, 1.5 mmol), titanium isopropoxide $Ti(OiPr)_4$ (0.305 mL, 1 mmol), and dodecanoic acid (6.06 g, 30 mmol) were introduced in a solution of 20 mL of *N,N*-dimethylformamide (DMF) and 2.2 mL of dry methanol. The mixture was stirred gently for 5 min at room temperature. After this, the reaction mixture was placed in a 25 mL reaction bottle and heated in an oven at 120 °C for 24 h. Back to room temperature, the yellow solid was separated by centrifugation, washed three times with DMF and twice with methanol, and dried under vacuum at 80 °C overnight.

UiO-66 nanoparticles were prepared following a synthetic procedure reported by Farha et. al.[47] In short, a stock solution of zirconyl chloride octahydrate in 30 mL DMF (210 mg, 0.9 mmol) was prepared. In a different vial, another stock solution of terephthalic acid in 10 mL of DMF (500 mg, 3.01 mmol) was prepared. Then in a reaction bottle, 1 mL of the terephthalic solution was added followed by the addition of 3 mL of the zirconyl solution. To this mixture, 1.4 mL of concentrated acetic acid (17.4 M) was added. Next, the sample was sonicated for 5 min to ensure complete mixing of reagents and then heated in an oven at 90 °C for 18 h, after which the sample was collected by centrifugation and washed once with DMF and two times with methanol.

ZIF-8 particles were prepared via a water-based synthesis reported earlier.[48a] Reactant solutions of 5 mL $Zn(OAc)_2{\cdot}4H_2O$ (0.55 M) and 5 mL of 2-Methylimidazole (5.5 M) in DI water were mixed and homogenized by vortexing. The mixed solution was left to react at room temperature under mild shaking for 24 h. The ZIF-8 crystals were collected after several washing steps using DI water.

Magnetic templates were prepared following the fabrication process reported by Mushtaq et.al.[42] Briefly, iron oxide nanoparticles were synthesized via a co-precipitation method. An aqueous solution of $FeCl_3$ (8 mM) and $FeCl_2$ (16 mM) was heated to 50 °C. Following dropwise addition of 0.5 M NaOH solution, a black suspension was formed and the mixture was sonicated for 60 min. The particles were then collected and 100 µL of 5 M HCl was added to bring the pH to the acidic range. *S. platensis* was used as biotemplate for the magnetic templates fabrication. Biotemplate coating was performed by incubating the templates with the iron oxide nanoparticles for 72 h under stirring. The coated biotemplates were collected after multiple wash steps. In the final wash step, the solution was instantly frozen in liquid nitrogen, and later freeze-dried overnight. The coated biotemplates were then annealed at 550 °C for 1.5 h. The annealed magnetic templates were stored in ambient conditions for future use. The gelatin–glycerol coating of the magnetic templates was performed as follows; 30 mg of gelatin were dissolved in 1 mL of water at 55 °C under continuous shaking at 800 rpm. 30 mL of glycerol were added along with 2 mg of magnetic templates. The mixture was homogenized for 10 min. Two washing steps (first with warm and then with cold water) were performed, before the solution of MOF particles (2 mg mL^{-1}) was introduced. Pre-synthesized MOF particles were implemented for all the biotemplated MOFBOTs fabrication. The coating time of the magnetic templates with the MOFs was 1 h. Multiple wash steps with water were then performed, and the final MOFBOTs were collected via magnetic separation.

Structural and Compositional Characterization: Scanning electron microscopy (SEM) images were obtained with SEM (Zeiss ULTRA 55 plus) operating at 5 kV. A drop of water dispersion of the sample was cast on Si chips that had previously been cleaned in acetone, isopropanol, and DI water. Once the water had evaporated, the samples were sputtered with a thin layer of Au, and imaging performed. An OXFORD instruments EDX detector was used for spot EDX and EDX mapping analysis. Transmission electron microscopy (TEM), scanning transmission electron microscopy (STEM), and EDX were performed with a FEI Talos F200X (Chem S/TEM) operating at 150 kV. Samples were prepared on carbon-coated Cu TEM grids (400 mesh). The crystalline phase was confirmed by X-ray diffraction (XRD) experiments on a PANalytical Empyrean X-ray platform (Cu radiation source) with PIXcel detector (Bruker AXS D8 Advance). IR spectra (cm^{-1}) were measured on an ATI Mattson Genesis Series FTIR instrument. TGA experiments were performed using TGA/DSC 3+ Star System, Mettler Toledo.

Magnetic Manipulation: Magnetic manipulation of the integrated MOFBOT was performed with a setup consisting of three pairs of orthogonally oriented Helmholtz coils, operating at 8–10 mT and and 0–20 Hz.

Cell Culture Experiments: Human breast cancer cells (MDA-MB-231) were cultivated in DMEM cell culture medium (10% FBS, 1 × Antibiotics-Antimycoticum) at physiological conditions (37 °C and 5% CO_2). Cell viability and DOX delivery experiments were performed in 48-multi-well plates. 10 000 cells were seeded in each well 24 h prior to treatment. On the day of treatment, the zero-time point, MIL-100(Fe) particles, magnetic templates, or MIL-100(Fe) MOFBOTs were introduced to the cell cultures. The cell viability percentage was calculated based on a MTT viability assay 24 h after treatment. For the MTT assay, 25 µL of MTT reagent and 3mg mL^{-1} of 3-(4,5-dimethylthiazol-2-yl)-2,5-diphenyl tetrazolium bromide in PBS at pH 7.4, were added to each well. Cells were incubated for 3 h. During this time, cells with an active metabolism converted the MTT reagent to a purple colored formazan crystal. The crystals were dissolved in DMSO, resulting in a purple colored solution. Absorbance was measured on a plate reader (TECAN, Infinite200Pro) with a test wavelength of 570 nm and a reference wavelength of 630 nm.

Cell Imaging: Bright field and fluorescence images were obtained using an Olympus IX-81 inverted optical microscope. LIVE/DEAD cell stain was used according to the manufacturer's protocol (Thermo Fisher Scientific, R37601).

RhB Degradation Experiments: The organic dye RhB served as a model organic pollutant. An initial concentration of 15 mg L^{-1} RhB in water solution was used for the experiments with MIL-125NH_2 particles. The MOF particle concentration in the solution was 1 mg mL^{-1}. The solution of RhB was incubated with MIL-125NH_2 nanocrystals for 2 h in darkness, to enable the absorption process to occur. The photocatalysis experiment was performed immediately after this and lasted 1 h. The equipment used for these experiments comprises a lamp MAX-303, Asahi Spectra, that operates with a filter MAX-UV–vis (300–600 nm). At each time step, a 200 µL aliquot was collected, and centrifuged at 12 000 rpm for 1 min. The supernatant was collected to indicate the concentration of RhB in the solution, whereas the pellet was further dissolved in EDTA solution (0.5 M, pH = 8), to give an estimate of the amount of RhB absorbed in the MIL-125NH_2 particles. The RhB concentration in solution was calculated from fluorescence intensity measurements using aTecan Infinite200Pro fluorimeter operating with an excitation wavelength of 556 nm and emission wavelength of 600 nm. RhB degradation experiments with MIL-125NH_2@MOFBOTs were performed following the same procedure. The initial RhB concentration was 10 mg L^{-1} and the magnetic templates or the MIL-125NH_2 MOFBOTs concentrations were 0.2 mg mL^{-1}.

Supporting Information

Supporting Information is available from the Wiley Online Library or from the author.

Acknowledgements

A.T., M.P.-C., and C.F. contributed equally to this work. This work was supported by the European Research Council under the ERC grant SOMBOT (No. 743217), ERC Consolidator Grant HINBOTS (No. 771565), ERC Starting Grant microCrysFact (No. 677020), the Swiss National Science Foundation (project no. 200021_181988) and grant PID2020-116612RB-C33 funded by MCIN/AEI/10.13039/501100011033. M.P. was supported by Ministry of Education, Youth and Sports (Czech Republic) grant LL2002 under ERC CZ program. C.M.G acknowledges funding from the Spanish Government (No. CEX2019-000919M and PID2020-118117RB-I00).

Conflict of Interest

The authors declare no conflict of interest.

Data Availability Statement

The data that support the findings of this study are available from the corresponding author upon reasonable request.

Keywords

biotemplating, microfabrication, microrobots, metal–organic frameworks

Received: July 29, 2021
Revised: October 8, 2021
Published online: December 7, 2021

[1] P. Ball, *Nature* **2000**, *406*, 118.
[2] K. D. Young, *Curr. Opin. Microbiol.* **2007**, *10*, 596.
[3] U. Hofer, *Nat. Rev. Microbiol.* **2019**, *17*, 528.
[4] A. Lee, *Scand. J. Gastroenterol., Suppl.* **1991**, *187*, 9.
[5] E. Yashima, N. Ousaka, D. Taura, K. Shimomura, T. Ikai, K. Maeda, *Chem. Rev.* **2016**, *116*, 13752.
[6] K. Das, L. Gabrielli, L. J. Prins, *Angew. Chem., Int. Ed.* **2021**, *60*, 20120.
[7] S. Chattopadhyay, R. Moldovan, C. Yeung, X. L. Wu, *Proc. Natl. Acad. Sci. USA* **2006**, *103*, 13712.
[8] E. M. Purcell, *Proc. Natl. Acad. Sci. USA* **1997**, *94*, 11307.
[9] J. E. Avron, O. Gat, O. Kenneth, *Phys. Rev. Lett.* **2004**, *93*, 186001.
[10] U. G. K. Wegst, H. Bai, E. Saiz, A. P. Tomsia, R. O. Ritchie, *Nat. Mater.* **2015**, *14*, 23.
[11] N. S. Ha, G. Lu, *Composites, Part B* **2020**, *181*, 107496.
[12] R. R. Naik, S. Singamameni, *Chem. Rev.* **2017**, *117*, 12581.
[13] S. Coyle, C. Majidi, P. LeDuc, K. J. Hsia, *Extreme Mech. Lett.* **2018**, *22*, 51.
[14] S. Palagi, P. Fischer, *Nat. Rev. Mater.* **2018**, *3*, 113.
[15] K. E. Peyer, L. Zhang, B. J. Nelson, *Nanoscale* **2013**, *5*, 1259.
[16] A. Ghanbari, *J. Micro-Bio Rob.* **2020**, *16*, 173.
[17] E. M. Purcell, *Am. J. Phys.* **1977**, *45*, 3.
[18] B. Rodenborn, C.-H. Chen, H. L. Swinney, B. Liu, H. P. Zhang, *Proc. Natl. Acad. Sci. USA* **2013**, *110*, E338.
[19] L. Zhang, J. J. Abbott, L. Dong, K. E. Peyer, B. E. Kratochvil, H. Zhang, C. Bergeles, B. J. Nelson, *Nano Lett.* **2009**, *9*, 3663.
[20] A. Chaiyasitdhi, W. Miphonpanyatawichok, M. O. Riehle, R. Phatthanakun, W. Surareungchai, W. Kundhikanjana, P. Kuntanawat, *PLoS One* **2018**, *13*, e0196383.
[21] S. Tottori, L. Zhang, F. Qiu, K. K. Krawczyk, A. Franco-Obregón, B. J. Nelson, *Adv. Mater.* **2012**, *24*, 811.
[22] H.-W. Huang, F. E. Uslu, P. Katsamba, E. Lauga, M. S. Sakar, B. J. Nelson, *Sci. Adv.* **2019**, *5*, eaau1532.
[23] K. J. Rao, F. Li, L. Meng, H. Zheng, F. Cai, W. Wang, *Small* **2015**, *11*, 2836.
[24] F. Qiu, B. J. Nelson, *Engineering* **2015**, *1*, 021.
[25] M. Sitti, H. Ceylan, W. Hu, J. Giltinan, M. Turan, S. Yim, E. Diller, *Proc. IEEE* **2015**, *103*, 205.
[26] J. Li, B. Esteban-Fernández de Ávila, W. Gao, L. Zhang, J. Wang, *Sci. Rob.* **2017**, *2*, eaam6431.
[27] B. Jurado-Sánchez, J. Wang, *Environ. Sci.: Nano* **2018**, *5*, 1530.
[28] M. Safdar, S. U. Khan, J. Jänis, *Adv. Mater.* **2018**, *30*, 1703660.
[29] H. Zhou, T. Fan, D. Zhang, *ChemSusChem* **2011**, *4*, 1344.
[30] Y. Ying, A. M. Pourrahimi, Z. Sofer, S. Matějková, M. Pumera, *ACS Nano* **2019**, *13*, 11477.
[31] S. Sotiropoulou, Y. Sierra-Sastre, S. S. Mark, C. A. Batt, *Chem. Mater.* **2008**, *20*, 821.
[32] J. Ali, U. K. Cheang, A. Darvish, H. Kim, M. J. Kim, *APL Mater.* **2017**, *5*, 116106.

[33] W. Gao, X. Feng, A. Pei, C. R. Kane, R. Tam, C. Hennessy, J. Wang, *Nano Lett.* **2014**, *14*, 305.
[34] H. Wang, M. G. Potroz, J. A. Jackman, B. Khezri, T. Marić, N. - J. Cho, M. Pumera, *Adv. Funct. Mater.* **2017**, *27*, 1702338.
[35] D. Wang, D. Chen, Z. Chen, *Front. Mater.* **2020**, *7*, 286.
[36] X. Wang, X.-H. Qin, C. Hu, A. Terzopoulou, X.-Z. Chen, T.-Y. Huang, K. Maniura-Weber, S. Pané, B. Nelson, *Adv. Funct. Mater.* **2018**, *28*, 1804107.
[37] A. Ghosh, P. Fischer, *Nano Lett.* **2009**, *9*, 2243.
[38] H.-W. Huang, M. S. Sakar, A. J. Petruska, S. Pané, B. J. Nelson, *Nat. Commun.* **2016**, *7*, 12263.
[39] R. Selvakumar, N. Seethalakshmi, P. Thavamani, R. Naidu, M. Megharaj, *RSC Adv.* **2014**, *4*, 52156.
[40] B. A. Krajina, A. C. Proctor, A. P. Schoen, A. J. Spakowitz, S. C. Heilshorn, *Prog. Mater. Sci.* **2018**, *91*, 1.
[41] A. Finamore, M. Palmery, S. Bensehaila, I. A. Peluso, *Oxid. Med. Cell. Longevity* **2017**, *2017*, 3247528.
[42] F. Mushtaq, X. Chen, S. Staufert, H. Torlakcik, X. Wang, M. Hoop, A. Gerber, X. Li, J. Cai, B. J. Nelson, S. Pané, *J. Mater. Chem. A* **2019**, *7*, 24847.
[43] X. Wang, X.-Z. Chen, C. C. J. Alcântara, S. Sevim, M. Hoop, A. Terzopoulou, C. d. Marco, C. Hu, A. J. d. Mello, P. Falcaro, S. Furukawa, B. J. Nelson, J. Puigmartí-Luis, S. M. Pané, *Adv. Mater.* **2019**, *31*, 1901592.
[44] A. Terzopoulou, X. Wang, X.-Z. Chen, M. Palacios-Corella, C. Pujante, J. Herrero-Martín, X.-H. Qin, J. Sort, A. J. de Mello, B. J. Nelson, J. Puigmartí-Luis, S. Pané, *Adv. Healthcare Mater.* **2020**, *9*, 2001031.
[45] C. Franco, D. Rodríguez-San-Miguel, A. Sorrenti, S. Sevim, R. Pons, A. E. Platero-Prats, M. Pavlovic, I. Szilágyi, M. L. Ruiz Gonzalez, J. M. González-Calbet, D. Bochicchio, L. Pesce, G. M. Pavan, I. Imaz, M. Cano-Sarabia, D. Maspoch, S. Pané, A. J. de Mello, F. Zamora, J. Puigmartí-Luis, *J. Am. Chem. Soc.* **2020**, *142*, 3540.
[46] M. Romero-Angel, J. Castells-Gil, V. Rubio-Giménez, R. Ameloot, S. Tatay, C. Martí-Gastaldo, *Chem. Commun.* **2021**, *57*, 9040.
[47] W. Morris, S. Wang, D. Cho, E. Auyeung, P. Li, O. K. Farha, C. A. Mirkin, *ACS Appl. Mater. Interfaces* **2017**, *9*, 33413.
[48] a) C. Avci, J. Ariñez-Soriano, A. Carné-Sánchez, V. Guillerm, C. Carbonell, I. Imaz, D. Maspoch, *Angew. Chem., Int. Ed.* **2015**, *54*, 14417; b) K. Liang, J. J. Richardson, J. Cui, F. Caruso, C. J. Doonan, P. Falcaro, *Adv. Mater.* **2016**, *28*, 7910; c) Z. Ji, H. Zhang, H. Liu, O. M. Yaghi, P. Yang, *Proc. Natl. Acad. Sci. USA* **2018**, *115*, 10582.
[49] Y. Li, C.-X. Yang, X.-P. Yan, *Chem. Commun.* **2017**, *53*, 2511.
[50] Z. Liu, C. Wang, Y. Wu, L. Geng, X. Zhang, D. Zhang, H. Hu, Y. Zhang, X. Li, W. Liu, P. Na, *Polyhedron* **2021**, *196*, 114980.
[51] B. V. Voorde, I. de Stassen, B. Bueken, F. Vermoortele, D. D. Vos, R. Ameloot, J.-C. Tan, T. D. Bennett, *J. Mater. Chem. A* **2014**, *3*, 1737.
[52] R. S. Malkar, H. Daly, C. Hardacre, G. D. Yadav, *React. Chem. Eng.* **2019**, *4*, 1790.
[53] C. Chautems, B. Zeydan, S. Charreyron, G. Chatzipirpiridis, S. Pané, B. J. Nelson, *Eur. J. Cardio-Thorac. Surg.* **2017**, *51*, 405.
[54] A. Terzopoulou, J. D. Nicholas, X.-Z. Chen, B. J. Nelson, S. Pané, J. Puigmartí-Luis, *Chem. Rev.* **2020**, *120*, 11175.
[55] B. Khezri, M. Pumera, *Adv. Mater.* **2019**, *31*, 1806530.
[56] C. R. Quijia, C. Lima, C. Silva, R. C. Alves, R. Frem, M. Chorilli, *J. Drug Delivery Sci. Technol.* **2021**, *61*, 102217.
[57] T. Baati, L. Njim, F. Neffati, A. Kerkeni, M. Bouttemi, R. Gref, M. F. Najjar, A. Zakhama, P. Couvreur, C. Serre, P. Horcajada, *Chem. Sci.* **2013**, *4*, 1597.
[58] J. Zhu, P.-Z. Li, W. Guo, Y. Zhao, R. Zou, *Coord. Chem. Rev.* **2018**, *359*, 80.
[59] Y. Fu, D. Sun, Y. Chen, R. Huang, Z. Ding, X. Fu, Z. Li, *Angew. Chem., Int. Ed.* **2012**, *51*, 3364.
[60] N. H. H. Hairom, A. W. Mohammad, L. Y. Ng, A. A. H Kadhum, *Desalin. Water Treat.* **2015**, *54*, 944.